Journal of Materials Chemistry A

ROYAL SOCIETY OF CHEMISTRY

PAPER

View Article Online
View Journal | View Issue

Cite this: J. Mater. Chem. A, 2024, 12, 3989

Effect of Pb 6s^2 lone pair on the potential flattening of fluoride-ion conduction in perovskite-type fluoride†

Naoki Matsui, *[a] Miwa Murakami, [b] Kazuhiro Mori, [c] Takashi Saito, [c] Keisuke Shimizu, [a] Kota Suzuki [a] and Ryoji Kanno*[a]

Materials containing ns^2 lone pairs exhibit superior fluoride-ion conductivity, acting as promising candidates for solid electrolytes in all-solid-state fluoride-ion batteries. However, the effect of lone pairs on fluoride-ion conduction remains unclear, especially for 6s^2 in Pb^{2+}. This study investigated the relationships between the ionic conductivity, crystal structure, and electronic structure of $CsPb_{0.9}K_{0.1}F_{2.9}$. Cubic $CsPb_{0.9}K_{0.1}F_{2.9}$ exhibited a low activation energy of 7.9 kJ mol^{-1}, resulting in high conductivity at 223 K (1.0×10^{-3} S cm^{-1}, bulk conductivity). ^{19}F nuclear magnetic resonance spectroscopy confirmed facile local migration of the fluoride ions with a low activation barrier of 3.8 kJ mol^{-1}. Theoretical calculations revealed that the fluoride ions migrated with a low migration energy *via* an exchange reaction between the Pb 6s lone pairs and fluoride ions. The localised lone pair in the PbF_5 polyhedron stabilised the saddle-point structure and mitigated the migration barrier. These findings are beneficial for material design, providing superionic conductivity with a low migration barrier for fluoride ions as well as other anions, such as oxide and chloride.

Received 19th October 2023
Accepted 9th January 2024

DOI: 10.1039/d3ta06367d

rsc.li/materials-a

Introduction

Materials containing cations with ns^2 ($n = 5$, 6) lone pair electrons, such as Pb^{2+}, Sn^{2+}, and Bi^{3+}, exhibit excellent macroscopic properties. Ferroelectric oxides of $PbTiO_3$ display superior dielectric properties, and perovskite-type $Na_{0.5}Bi_{0.5}TiO_3$ and layered fluorite-type $PbSnF_4$ exhibit high anion conductivities.[1–3] These cations with lone pairs possess high electronic polarisability.[4] The larger the polarisation of the lattice ions in the same structure, the lower the activation barrier for ionic conduction of the carrier ion.[5] Several superior anion conductors have been found in polarisable cation systems with ns^2 valence electron configuration.[1,6–11] Particularly, the demand for the fluoride-ion conductors as solid electrolytes for use in all-solid-state fluoride-ion batteries (ASSFIBs) has increased.[12] ASSFIBs exhibit high energy density, making them suitable candidates for post-lithium-ion batteries.[13] Fluoride-ion conductors exhibiting high conductivity in a wide temperature range are essential to achieve ASSFIBs with high power densities and wide operating temperature ranges. Various crystal structures are known for fluoride-ion conductors, such as fluorite-type $MSnF_4$ (M = Pb, Ba)[14,15] and $Pb_{1-x}M_xF_{2\pm\delta}$ (M = K, Zr),[16,17] perovskite-type $APbF_3$ (A = Cs, Rb),[9,18] and ASn_2F_5-type compounds (A = Na–Cs, Tl, and NH_4).[19] Ternary tin fluorides with open space in their structures, such as $PbSnF_4$ and ASn_2F_5, exhibit high fluoride-ion conductivities above 10^{-4} S cm^{-1}. The strong stereochemical activity of the Sn 5s^2 lone pair leads to its localisation, resulting in an asymmetric local structure.[20] Therefore, fluorides containing Sn^{2+} possess open spaces in their structures. The effect of the Sn^{2+} lone pair on the fluoride-ion conductivity has been investigated in $MSnF_4$ (M = Pb, Ba),[21] wherein the lone pair of Sn^{2+} pushes the F away from the tetrahedral towards octahedral sites, forming the Frenkel defect pair F_i and V_F, which are interstitial F and F vacancies, respectively. In the layered fluorite-type $PbSnF_4$, the cations stack in the [Pb–Pb–Sn–Sn] manner along the *c*-axis in the tetragonal lattice. G. Dénès *et al.* systematically investigated the coordination environment and charge density of Sn^{2+} using neutron diffraction and ^{119}Sn Mössbauer spectroscopy.[23,24] According to their research, the stereoactive lone pair of Sn is oriented to the [Sn–Sn] interlayer along the *c*-axis in tetragonal $PbSnF_4$. The fluoride ions disappear in the [Sn–Sn] interlayer; however, they occupy the interstitial sites in the [Pb–Sn] interlayer. This arrangement enables concerted fluoride-ion migration involving interstitial sites with a low activation energy.[22] In contrast, the role of the Pb 6s^2 lone pair in fluoride-ion conduction remains unclear.

[a]Research Center for All-Solid-State Battery, Institute of Innovative Research, Tokyo Institute of Technology, 4259 Nagatsuta-cho, Midori-ku, Yokohama 226-8502, Japan. E-mail: matsui.n.aa@m.titech.ac.jp; kanno.r.ab@m.titech.ac.jp

[b]Office of Society-Academia Collaboration for Innovation, Kyoto University, Gokasho, Uji, Kyoto 611-0011, Japan

[c]Institute of Materials Structure Science, High Energy Accelerator Research Organization (KEK), 203-1 Shirakata, Tokai, Ibaraki 319-1106, Japan

† Electronic supplementary information (ESI) available. See DOI: https://doi.org/10.1039/d3ta06367d

The stereochemical activity of $6s^2$ in Pb^{2+} is relatively low compared to that of $5s^2$ in Sn^{2+}.[20] Consequently, no defect structure is present in the lead fluoride system, and the effect of the $6s^2$ lone pair on the conductivity is overlooked. Cubic perovskite-type $CsPbF_3$, in which Cs^+ and Pb^{2+} occupy A- and B-sites, respectively, exhibit high ionic conductivity on the order of 10^{-5} S cm^{-1} at room temperature.[9] Recently, exceptionally high ionic conductivity of the order 10^{-3} S cm^{-1} was reported for $CsPb_{0.9}K_{0.1}F_{2.9}$.[25] The F vacancy introduced *via* the substitution of K^+ at the host Pb^{2+} site triggered fast fluoride-ion conduction. However, the detailed conduction mechanism in addition to the effect of the lone pair remains unclear. This study investigated the ionic conductivities and crystal structures of $CsPbF_3$ and $CsPb_{0.9}K_{0.1}F_{2.9}$ in detail using impedance spectroscopy and neutron diffraction measurements. Additionally, the F dynamics was studied using nuclear magnetic resonance (NMR) spectroscopy. Furthermore, the effect of the lone pair of Pb^{2+} ions on the high fluoride-ion conductivity was elucidated using first-principles calculations. This study provides new insights into the mechanism through which migration energies are mitigated in Pb-perovskite systems.

Experimental

Synthesis

$CsPbF_3$ and $CsPb_{0.9}K_{0.1}F_{2.9}$ were prepared *via* mechanochemical synthesis. The starting materials, CsF, PbF_2, and KF, were weighed in an Ar-filled glove box and subjected to mechanochemical milling (zirconia pot with a volume of 45 mL and 18 balls of diameter 10 mm) in an Ar atmosphere for 12 h at 600 rpm using a planetary ball mill (Fritsch, P-7). The obtained sample was enclosed in an airtight Cu capsule under an Ar atmosphere and then annealed at 473 K for 12 h.

Characterisation

The ionic conductivities were determined using alternating current (AC) impedance spectroscopy. The sample was compressed to a diameter of 10.0 mm, thickness of approximately 1 mm, and relative density of over 90% under a pressure of 340 MPa. The Pt sheets were used as current collectors. The AC impedance measurements were performed using a frequency response analyser (Keysight E4990A) at an applied voltage of 10 mV and a frequency range of 100 MHz–20 Hz in the 423–173 K temperature range. The activation energy (E_a) was obtained using the Arrhenius equation, $\sigma = A_0/T\exp(-E_a/kT)$, where A_0, k, and T are pre-exponential factor, Boltzmann constant, and absolute temperature, respectively.

Synchrotron X-ray diffraction data were collected at the BL02B2 beamline within the SPring-8 facility.[26] Diffraction data were collected in the 2–75° 2θ range using a Debye–Scherrer diffraction camera. Neutron powder diffraction (NPD) data were acquired using a time-of-flight neutron powder diffractometer (BL09 SPICA) at the J-PARC facility.[27] The crystal structures were refined *via* Rietveld analysis using the computer programs Z-Rietveld and RIETAN-FP.[28,29] The nuclear scattering length density distribution was analysed through the maximum entropy method (MEM) using the Z-MEM code.[30] The NMR measurements were performed using a JEOL ECA600 NMR spectrometer at 14 T with the triply tuned magic-angle spinning (MAS) probe (Agilent Technologies Inc.) with a 1.6 mm rotor. The resonance frequencies for ^{19}F and ^{207}Pb were 564 and 126 MHz, respectively. The ^{19}F chemical shifts were calibrated in ppm relative to CCl_3F, employing the ^{19}F chemical shift for C_6F_6 (−163 ppm (ref. 31)) as an external reference. The ^{207}Pb chemical shifts were calibrated in ppm relative to a saturated aqueous solution of $Pb(NO_3)_2$. The temperature-calibration experiment was conducted using ^{207}Pb NMR of $Pb(NO_3)_2$.[32] The NMR spectra of ^{19}F and ^{207}Pb were observed using a single pulse with the Hahn echo under MAS at 35 kHz. Application of ^{19}F decoupling showed no appreciable narrowing effects on the ^{207}Pb spectra (not shown). The two-dimensional (2D) exchange NMR experiment was performed with the conventional three-pulse sequence.[33] The spin–lattice relaxation time (T_1) was obtained using the saturation-recovery method under MAS. The ^{207}Pb T_1 was also measured at 4.7 T by utilizing an OPENCORE spectrometer.[34]

Calculation

First-principles density functional theory calculations were performed using the projector-augmented wave method[35] and the PBEsol functional[36] as implemented in the Vienna *Ab initio* Simulation Package code.[37,38] Firstly, geometrical optimisation of the unit cell of $CsMF_3$ (M = Pb, Sr) was conducted. The energy cutoff was set to 520 eV for structural optimisation. The Cs 5s5p6s, Pb 6s6p, Sr 4s4p5s, and F 2s2p orbitals were treated as valence states. The total energies and forces converged to less than 1×10^{-5} eV, and the force criterion was 0.01 eV Å^{-1}. Nudged elastic band (NEB) calculation, the most convenient method for finding the saddle point and path that requires the least energy, was performed for the F^- vacant supercell with an energy cutoff at 400 eV. Five intermediate points were considered in the NEB calculations. A $2 \times 2 \times 2$ supercell with a gamma-centred $2 \times 2 \times 2$ k-mesh was used. The F^- vacancy was charge-compensated by removing eight electrons from the valence electrons in the supercell. The densities of states (DOSs) for the initial, intermediate, and endpoint structures in the NEB calculations were determined using the hybrid exchange–correlation functional (HSE06).[39–41] The partial electron density was analysed for states between −10 eV and the Fermi level. The crystal structures and electron densities were visualised using visualisation for electronic and structural analysis.[42]

Results and discussion

Fig. 1(a)–(c) show the Nyquist plots of $CsPb_{0.9}K_{0.1}F_{2.9}$ at 298, 248, and 203 K, respectively. Two semicircles with capacitances of 3×10^{-11} and 1×10^{-8} F, corresponding to the bulk and grain-boundary resistances, respectively, are observed in the high frequency region. The bulk and grain boundary resistances were calculated by fitting the Nyquist plots to the equivalent circuit, as shown in Fig. 1(d). The total ionic conductivity was obtained by taking the sum of the bulk and grain boundary

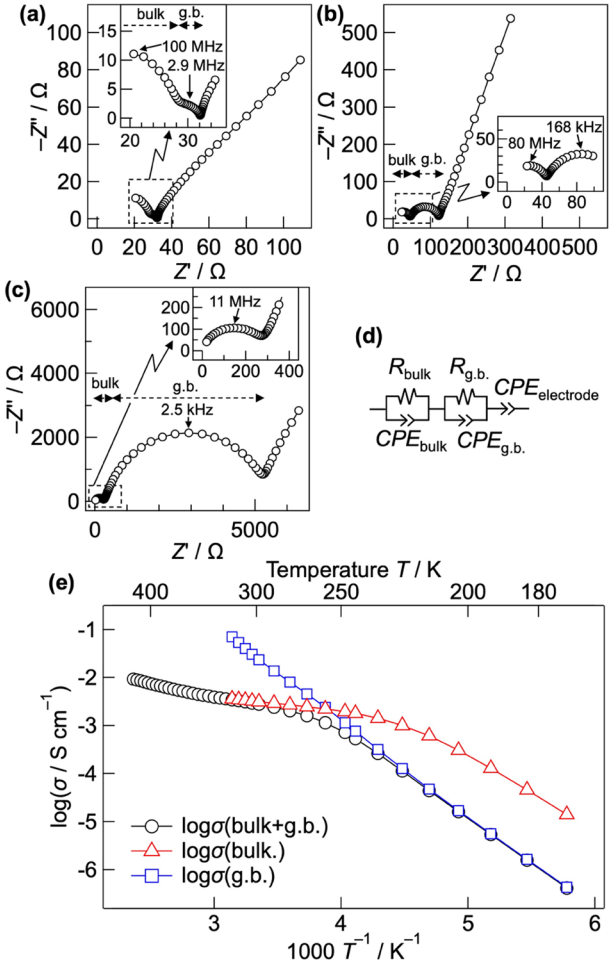

Fig. 1 Nyquist plot of $CsPb_{0.9}K_{0.1}F_{2.9}$ at (a) 298 K, (b) 248 K, and (c) 203 K. The dashed horizontal arrows represent the bulk and grain boundary resistances. Expansions of the high frequency regions are shown in the insets. (d) Equivalent circuit for fitting the observed data points. (e) Arrhenius plot of the ionic conductivities of $CsPb_{0.9}K_{0.1}F_{2.9}$. The bulk, grain boundary (g.b.), and total conductivities are shown as red triangles, blue squares, and black circles, respectively.

resistances. Above 323 K, the total conductivity was calculated solely from the bulk resistance owing to the difficult separation of the grain boundary resistance. Fig. 1(e) shows the Arrhenius plot of the ionic conductivity of $CsPb_{0.9}K_{0.1}F_{2.9}$. Table S1† summarises the conductivities and activation energies of the bulk, grain boundary, and total conductivities. The total conductivity is 2.7×10^{-3} S cm^{-1} at 298 K, which is comparable to the previously reported value of 1.2×10^{-3} S cm^{-1}.[25] A low activation energy of 10.89(4) kJ mol^{-1} for the total conductivity is observed in the 298–348 K range, similar to those of the superionic conductors α-Ag_3SI (13–19 kJ mol^{-1})[43,44] and $PbSnF_4$ (10 kJ mol^{-1}).[1] At temperatures below 258 K, the activation energy increases to 37.62(17) kJ mol^{-1}, considerably decreasing the total conductivity. The increased activation energy can be explained by the change of the dominant component of the resistance from the bulk to the grain-boundary resistance, as shown in Fig. 1(b) and (c). The bulk conductivity is 3.1×10^{-3} S cm^{-1} at 298 K, with an exceptionally low activation energy of 7.92(9) kJ mol^{-1}. Owing to this low activation energy, high ionic conductivity is maintained even at temperatures lower than room temperature, with a bulk conductivity of 1.0×10^{-3} at 223 K. At temperatures below 233 K, the activation energy of the bulk conductivity spontaneously increases to 31.8(5) kJ mol^{-1}. This increase is attributed to the displacive phase transition from a cubic to a tetragonal system, as discussed later. In contrast, the grain boundary conductivity consistently follows the Arrhenius-law in the wide temperature range of 173–318 K, yielding an activation energy of 40.0(2) kJ mol^{-1}. For comparison, the ionic conductivity of $CsPbF_3$ was evaluated, as shown in Fig. S1.† The total conductivity is 2.1×10^{-4} S cm^{-1} at 298 K, which is one order of magnitude lower than that of $CsPb_{0.9}K_{0.1}F_{2.9}$. The activation energy is 7.1(2) kJ mol^{-1} for the bulk conductivity in the 193–233 K temperature range. The low activation energies of $CsPbF_3$ and $CsPb_{0.9}K_{0.1}F_{2.9}$ reflect an intrinsically low migration barrier for the fluoride-ion conduction in $CsPbF_3$, whereas the enhanced conductivity of $CsPb_{0.9}K_{0.1}F_{2.9}$ is attributable to the increased carrier concentration, *i.e.* F vacancies.

Fig. 2(a) shows the low temperature XRD patterns of $CsPb_{0.9}K_{0.1}F_{2.9}$. With decreasing temperature, the symmetry changes at 225 K, represented by splitting of the *hh*0 reflection into two (Fig. 2(b)). Fig. 2(c) depicts the temperature dependence of the lattice parameters. Cubic $CsPb_{0.9}K_{0.1}F_{2.9}$ exhibits monotonic thermal expansion in the 250–450 K temperature

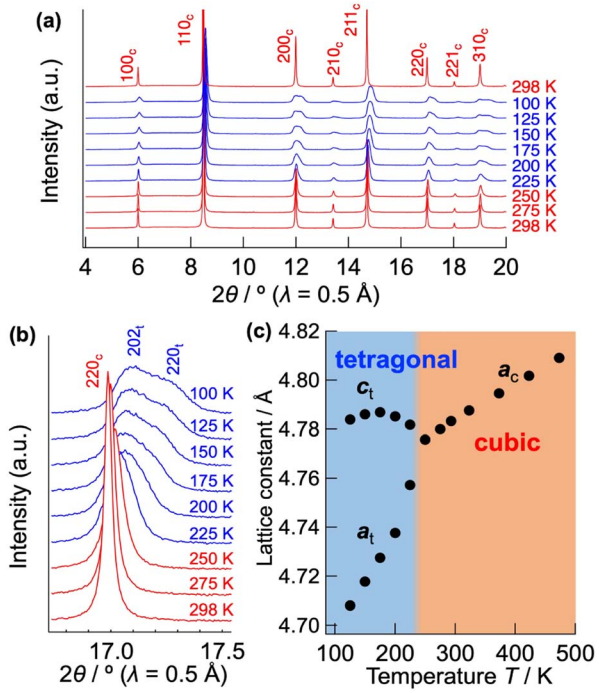

Fig. 2 (a) Low temperature XRD patterns of $CsPb_{0.9}K_{0.1}F_{2.9}$, recorded between 298 K and 100 K. (b) Expansion of the 220 reflection. The diffraction patterns exhibiting cubic and tetragonal phases are displayed as red and blue lines, respectively. Mirror indices are given for each Bragg reflection, representing the cubic and tetragonal crystal systems as c and t, respectively. (c) Temperature dependence of the lattice parameters of $CsPb_{0.9}K_{0.1}F_{2.9}$.

range. Conversely, it undergoes a phase transition to the tetragonal phase associated with a contraction of the *a*-axis and an expansion of the *c*-axis from 225 to 175 K. Fig. S2(a)† presents the Rietveld refinement results for tetragonal $CsPb_{0.9}K_{0.1}F_{2.9}$ at 200 K. In tetragonal $CsPb_{0.9}K_{0.1}F_{2.9}$ with a space group of *P*4*mm*, the B-site Pb^{2+} is marginally displaced from the PbF_6 octahedral centre ($z(Pb^{2+}) \approx 0.47$), elongating the *c*-axis ($a \approx 4.71$ Å, $c \approx 4.78$ Å, Fig. S2(b) and Table S2†). Off-centred Pb^{2+} has been previously observed in other perovskite halides[45] owing to the localised $6s^2$ lone pair of Pb^{2+}. Additionally, the *P*4*mm* space group is consistent with that of ferroelectric $PbTiO_3$. In contrast, the bare $CsPbF_3$ undergoes a phase transition from a cubic to a rhombohedral structure at 185 K, featuring PbF_6 octahedra tilting.[9] This phase transition is supported by a sudden decrease in the ionic conductivity from 188 to 183 K for $CsPbF_3$ (Fig. S1†). However, such a transition is absent in $CsPb_{0.9}K_{0.1}F_{2.9}$. The different low temperature forms, tetragonal $CsPb_{0.9}K_{0.1}F_{2.9}$ and rhombohedral $CsPbF_3$, can be attributed to fluoride ion vacancies. Given the presence of open space in the structure, the Pb lone pair preferentially localises to fill this open space.[46] The fluoride-ion vacancy in $CsPb_{0.9}K_{0.1}F_{2.9}$ can induce the stereochemical activity of Pb 6s, stabilising the tetragonal form by orienting the lone pair along its *c*-axis while displacing Pb^{2+} along the opposite direction. The tetragonal form possesses two crystallographically non-equivalent F sites, resulting in an anisotropic energy landscape for fluoride-ion conduction. In contrast, within the cubic structure of $CsPb_{0.9}K_{0.1}F_{2.9}$, the lone pair of Pb is expected to be randomly oriented, providing an isotropic conduction pathway. This displacive phase transition from a cubic to a tetragonal system in $CsPb_{0.9}K_{0.1}F_{2.9}$ is responsible for the spontaneous change in the activation energy of the bulk conductivity below 233 K (Fig. 1(e)).

Fig. 3(a) shows the Rietveld analysis results for the neutron powder diffraction data for cubic $CsPb_{0.9}K_{0.1}F_{2.9}$ (see Table 1 for the structural parameters). The presence of 9% K at the Pb site and approximately 3% vacancies at the F site ensure charge compensation of the F vacancies for K substitution at the Pb site. The atomic displacement parameter (ADP) of F is large, $U_{eq} = 0.0835(2)$ Å^2. Additionally, the ADP of F exhibits remarkable anisotropy, with $U_{22} = 0.0990(3)$ and $U_{11} = 0.0525(4)$ Å^2. The large U_{22} value for F corresponds to a substantial displacement perpendicular to the Pb–F bond. The large U_{22} value is confirmed for un-doped $CsPbF_3$ (see Fig. S3†), which features an intrinsically flat energy landscape for F towards neighbouring sites in $CsPbF_3$. Fig. 3(c) presents the nuclear density distribution obtained using MEM. MEM analysis reproduces the wide distribution of F perpendicular to the Pb–F bond direction. No other nuclear densities corresponding to interstitial F are observed. The nuclear density for the Pb site shows a non-spherical shape spreading towards neighbour F sites, whereas Pb exhibits a spherical shape in the density map of $CsPbF_3$ (Fig. S3(c)†). The non-spherical shape of the Pb site in $CsPb_{0.9}K_{0.1}F_{2.9}$ could be attributed to the static disorder of Pb owing to the K^+-substitution, which was detected in the NMR study discussed later. In addition to the presence of vacancies at the F site, the broad distribution of F towards adjacent sites

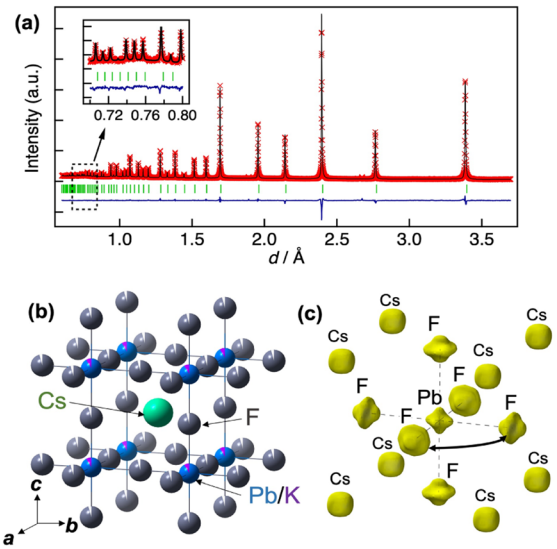

Fig. 3 (a) Rietveld refinement result for neutron diffraction data of $CsPb_{0.9}K_{0.1}F_{2.9}$ at 298 K. The red crosses, black line, blue line, and green marks represent the observed intensities, calculated intensities, difference curve, and positions of the Bragg reflections of cubic-$CsPb_{0.9}K_{0.1}F_{2.9}$, respectively. (b) Refined structure of $CsPb_{0.9}K_{0.1}F_{2.9}$. The green, blue, purple, and grey balls represent Cs, Pb, K, and F atoms, respectively. (c) Three-dimensional isosurface of nuclear scattering length density of $CsPb_{0.9}K_{0.1}F_{2.9}$ obtained using MEM analysis. The yellow isosurfaces correspond to the positive nuclear scattering length density at 5 fm Å^{-3}.

suggests that fluoride ions diffuse *via* single hopping between adjacent F sites along the edges of the PbF_6 octahedron.

To explore the origin of the low activation energy for fluoride-ion conduction in $CsPbF_3$, NEB calculations were performed. Fig. 4 shows the migration barrier of fluoride ions between adjacent F sites through vacancy-mediated hopping in cubic $CsPbF_3$ obtained using NEB calculations. The estimated migration barrier is 8 kJ mol^{-1}, which is close to the experimental value, $E_a = 7.1(2)$ kJ mol^{-1}. For comparison, the migration barrier of fluoride ions for $CsSrF_3$ was calculated, in which Sr^{2+} at the B site has a similar ionic radius ($r_{Sr^{2+}} = 1.18$ Å and $r_{Pb^{2+}} = 1.19$ Å)[47] and lacks ns^2 electrons within the valence electron configuration (Fig. S4†). $CsSrF_3$ exhibits a relatively high migration barrier of 35 kJ mol^{-1}, highlighting the effect of ns^2 electrons in the B-site cations, which facilitate reduction of the migration barrier.

Fig. 5 shows the partial density of states (PDOS) for $CsPbF_3$, including one F^- vacancy corresponding to the initial state of the NEB calculation. The valence band comprises three regions. The first region near the Fermi level primarily comprises the F 2p orbital with the hybridisation of the Pb 6s orbital. The other F 2p orbitals are located below −4 eV, partly hybridising the Cs 5p and Pb 6p orbitals in the second region. The third region around −8 eV encompasses contributions from Pb 6s and Cs 5p orbitals, in addition to a small amount of F. The partial electron densities were analysed for states between −10 eV and the Fermi level to gain deeper insight into the role of the lone pair in the conduction mechanism. Fig. 6(a)–(f) present the cross-

Table 1 Rietveld refinement results from the neutron diffraction data of $CsPb_{0.9}K_{0.1}F_{2.9}$ ($CsPb_{0.91}K_{0.09}F_{2.91}$) at 298 K[a]

Atom	Site	g	x	y	z	U_{eq}/Å^2	U_{11}/Å^2	U_{22}/Å^2	U_{33}/Å^2
Cs	1b	1	0.5	0.5	0.5	0.03932(15)	0.03932(15)	$=U_{11}$(Cs)	$=U_{11}$(Cs)
Pb	1a	0.910(2)	0	0	0	0.019105(10)	0.019105(10)	$=U_{11}$(Pb)	$=U_{11}$(Pb)
K	1a	$=1-g$(Pb)	0	0	0	$=U_{eq}$(Pb)	$=U_{11}$(Pb)	$=U_{11}$(Pb)	$=U_{11}$(Pb)
F	3d	0.9701(7)	0.5	0	0	0.0835(2)	0.0525(4)	0.0990(3)	$=U_{22}$(F)

[a] Unit cell: cubic $Pm\bar{3}m$ (221); $a = b = c = 4.788192(6)$ Å, $R_{wp} = 3.51\%$, $R_e = 2.19\%$, $R_p = 3.11\%$, $R_B = 4.21\%$, $R_F = 6.28\%$, goodness of fit $S = R_{wp}/R_e = 1.60$.

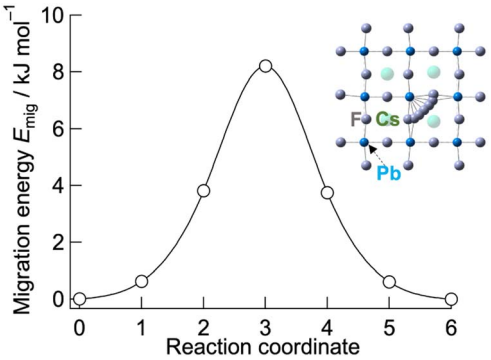

Fig. 4 Migration energy of fluoride ions in cubic $CsPbF_3$. The migrating fluoride ions corresponding to the reaction coordinate are depicted in the inset.

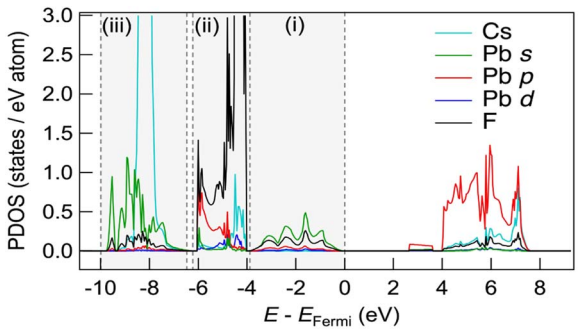

Fig. 5 PDOS of the supercell of $CsPbF_3$ with an F-defective structure. Three valence band regions are surrounded by dashed vertical lines.

sectional contour and isosurface plots, respectively, of the partial electron density during fluoride-ion migration in $CsPbF_3$. The stereochemical activity of Pb 6s depends on its coordination environment. In the initial structure, the electron density of Pb in the PbF_5 square pyramid adjacent to the F vacancy is asymmetric and localised in the direction of the F vacancy (V_F). In contrast, the electron density of Pb in the PbF_6 octahedral region, which is not adjacent to the F vacancy, is symmetrical and delocalised. Walsh reported similar selectivity for the stereochemical activity of Pb 6s electrons, where Pb 6s in the PbO_6 octahedra of rock salt-type PbO was delocalised.[46] Conversely, Pb 6s in the distorted PbO_8 hexahedra is asymmetrically localised towards open space in litharge-type PbO. Similarly, Pb 6s becomes stereochemically active when five F atoms coordinate with Pb in F-defective $CsPbF_3$, localising the 6s lone pair towards open space at F-vacant sites. During the transition state, one fluoride ion in the PbF_6 octahedron cleaves the Pb–F bond and passes through a bottleneck comprising 1 × Pb and 2 × Cs. The former delocalised Pb electron density in the PbF_6 octahedra localises towards the new V_F created by the cleavage of the Pb–F bond. Furthermore, the electron density of Pb in the PbF_5 trigonal bipyramid labelled as (iii) in Fig. 6(e) is marginally localised in the opposite direction to the travelling F. In the endpoint structure, the travelling F is associated with the PbF_5 square pyramid to form a PbF_6 octahedron, delocalising the Pb electron density. These results confirm that fluoride ions are carried by the exchange reaction between the fluoride ions and the Pb 6s lone pair localised in the V_F. Fig. 6(g) shows the site-projected PDOS of the PbF_6 octahedra and three PbF_5 polyhedra: (i) and (ii) square pyramids and (iii) a trigonal bipyramid. The region near the Fermi level of PbF_6 is occupied by Pb 6s and F 2p electrons. In contrast, in the PbF_5 polyhedron, the DOS of Pb shifts to the lower-energy side (as indicated by the dashed line), stabilising the Pb 6s state and PbF_5 geometry. One V_F and two PbF_5 geometries exist in the initial structure, but two V_F and three PbF_5 geometries are present in the transition structure. The three stable PbF_5 polyhedral geometries in the transition state stabilise the structure and reduce the migration barrier of fluoride ions.

Further, high resolution $^{19}F/^{207}Pb$ NMR spectroscopy was used to explore the F dynamics correlated with Pb in $CsPb_{0.9}K_{0.1}F_{2.9}$. Fig. 7 compares the ^{19}F and ^{207}Pb MAS NMR spectra of $CsPbF_3$ and $CsPb_{0.9}K_{0.1}F_{2.9}$. The narrower ^{19}F line shape for $CsPb_{0.9}K_{0.1}F_{2.9}$ indicates efficient motional narrowing, which is consistent with its better ionic conductivity. The ^{207}Pb spectrum of $CsPbF_3$ is a simple Lorentzian reflecting better local symmetry in the unit cell than that of the $CsPb_{0.9}K_{0.1}F_{2.9}$, which exhibits substantial broadening. The broad line shape does not depend on temperature up to 100 °C (not shown). To explore the nature of this broadening, a 2D exchange spectrum at 80 °C with a mixing time of 50 ms was obtained (Fig. 8), in which only the narrow diagonal signal exists. This finding indicates that the broad linewidth in the 1D spectrum is a sum of an individual sharp signal with its isotropic chemical shift distributed over 1000–1800 ppm, approximately. Further, the absence of off-diagonal signals indicates that exchange among these broadly distributed ^{207}Pb signals is less evident in 50 ms at 80 °C. The linewidth of each ^{207}Pb spin isochromat is separately observed *via* the Hahn-echo sequence to be 470 Hz ($T_2 \sim 0.68(3)$ ms), which is consistent with the narrow diagonal signal in

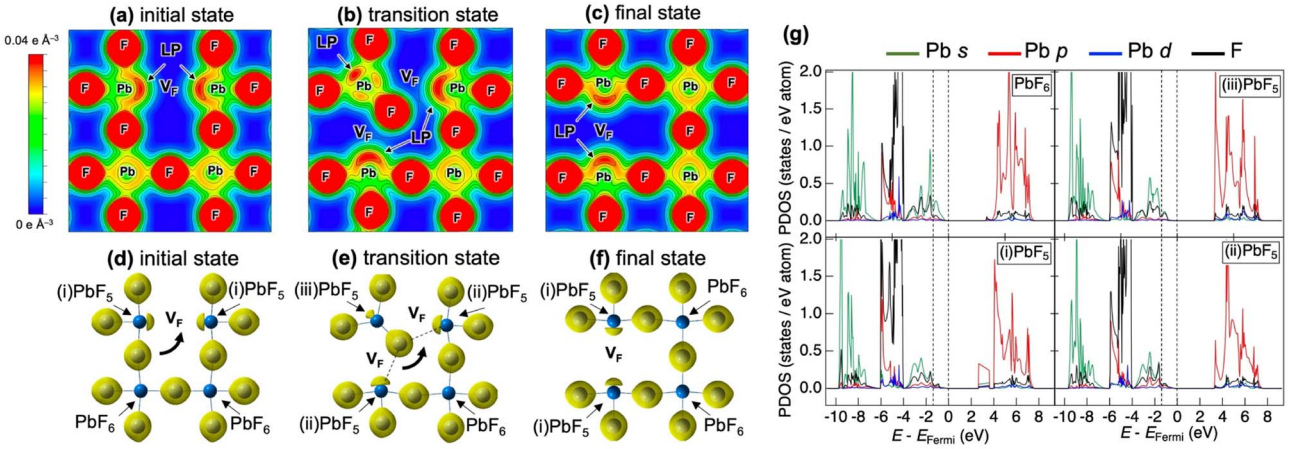

Fig. 6 (a–c) Contour plots of the cross-section of the (100) plane and (d–f) isosurface plots of partial electron density from −10 eV to the Fermi level of $CsPbF_3$. (a and d) Initial, (b and e) transition, and (c and f) final states of the fluoride-ion migration *via* adjacent F-vacancy in the NEB calculation. The contour plots are drawn from 0 to 0.04 e Å^{-3} with a 0.005 e Å^{-3} interval. The three-dimensional isosurfaces of 0.035 e Å^{-3} are depicted in yellow. (g) Site-projected PDOS of Pb and F in PbF_6 and three PbF_5 polyhedrons. The valence band region near the Fermi level is represented by the dashed vertical line.

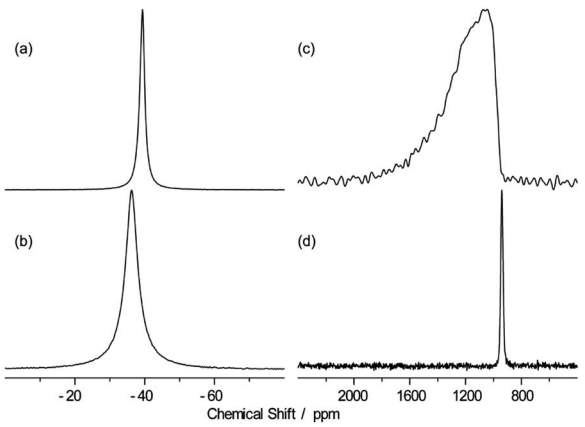

Fig. 7 ^{19}F (a and b) and ^{207}Pb (c and d) MAS spectra of $CsPbF_3$ (b and d) and $CsPb_{0.9}K_{0.1}F_{2.9}$ (a and c) with the MAS frequency of 25 kHz at 40 °C.

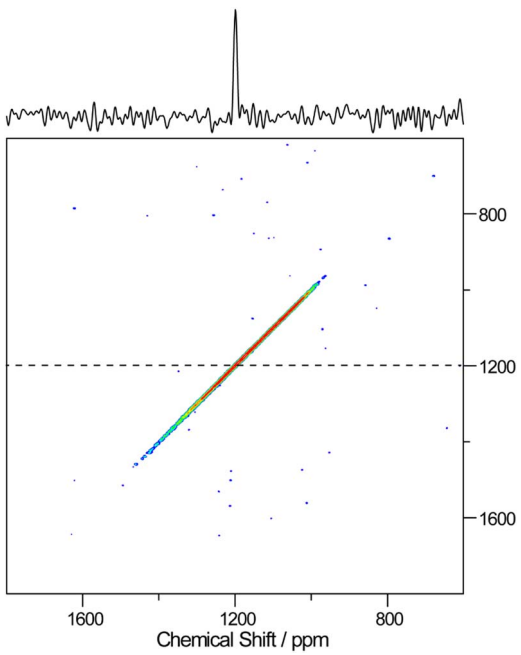

Fig. 8 ^{207}Pb–^{207}Pb 2D-exchange spectrum of $CsPb_{0.9}K_{0.1}F_{2.9}$ obtained at 80 °C with a mixing time of 50 ms. The cross-section spectrum at 1200 ppm is represented by the dashed line at the top.

Fig. 8. The broad distribution of the isotropic chemical shift of ^{207}Pb in $CsPb_{0.9}K_{0.1}F_{2.9}$ is attributed to the variation of the local structure of the Pb atom owing to 10% K^+ substitution on the Pb site. The distortion of the Pb site is observed as non-spherical nuclear density obtained using the MEM analysis (Fig. 3(c)). The ^{207}Pb chemical shift is sensitive to its local structure, leading to the wide chemical shift range from −6000 to 6000 ppm.[48]

The absence of exchange among the different Pb sites in $CsPb_{0.9}K_{0.1}F_{2.9}$ as confirmed by the 2D-exchange NMR experiment establishes that the broad distribution of the chemical shift of ^{207}Pb is due to the variation of the configuration between Pb and immobile K rather than mobile F (or F vacancy). The dynamics of Pb and F by T_1 were examined further. At first, the anisotropy of ^{207}Pb-T_1 for the broadly distributed peaks of $CsPb_{0.9}K_{0.1}F_{2.9}$ was ignored and ^{207}Pb-T_1 was obtained from the recovery curve for the whole signal. Fig. 9 shows the temperature dependence of T_1 of ^{19}F and ^{207}Pb in $CsPbF_3$ and $CsPb_{0.9}K_{0.1}F_{2.9}$. The ^{19}F-T_1 of $CsPbF_3$ shows that fluoride-ion motion is too slow to affect T_1 below 20 °C. The 10% K^+ substitution reduces the ^{19}F-T_1 of $CsPb_{0.9}K_{0.1}F_{2.9}$ by more than one order of magnitude, indicating better fluoride-ion mobility in $CsPb_{0.9}K_{0.1}F_{2.9}$. The slope of $\log(T_1)$ *vs.* $1/T$ gives an activation energy of 3.8(1) kJ mol^{-1}, which is much smaller than the value of 7.92(9) kJ mol^{-1} obtained from the temperature dependence of the bulk ionic conductivity in the similar temperature range. It appears that the motion governing ^{19}F T_1 is local with smaller

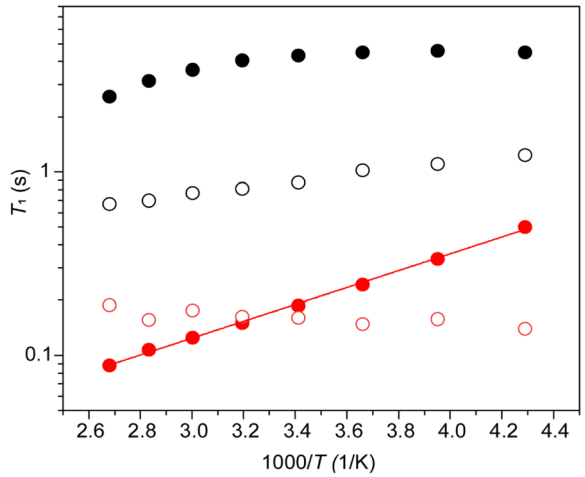

Fig. 9 Temperature dependence of the ^{19}F (●) and ^{207}Pb (○) spin–lattice relaxation times (T_1) for $CsPbF_3$ (black) and $CsPb_{0.9}K_{0.1}F_{2.9}$ (red). The straight line through the ^{19}F T_1 data points for $CsPb_{0.9}K_{0.1}F_{2.9}$ is $T_1 \propto \exp(E_a/kT)$ with $E_a = 3.8$ kJ mol^{-1}.

activation energies. The T_1 of immobile ^{207}Pb is smaller than that of mobile ^{19}F for $CsPbF_3$ and ^{207}Pb-T_1 ~ ^{19}F-T_1 for $CsPb_{0.9}K_{0.1}F_{2.9}$. Short T_1 has been reported for ^{119}Sn spin in $PbSnF_4$,[49] in which the $5s^2$ lone pair of Sn^{2+} is stereochemically active and the fluctuating chemical-shielding anisotropy (CSA) invokes the relaxation. To confirm that the ^{207}Pb-T_1 is governed by the fluctuation of CSA, the ^{207}Pb-T_1 of $CsPb_{0.9}K_{0.1}F_{2.9}$ was observed at 4.7 T. The observed ^{207}Pb-T_1 at 40 °C is 0.43 s, which is longer than that observed at 14 T (0.16 s). The ratio 0.43/0.16 is close to the ratio of the strength of the static field (14/4.7), confirming the relaxation mechanism being the fluctuation of CSA. The CSA relaxation is consistent with the exchange model among the fluoride ions and the F vacancies, as illustrated in Fig. 6(d)–(f). It should be mentioned here that a simple F–F mutual exchange around a ^{207}Pb spin does not affect the CSA of the ^{207}Pb spin and the fluctuation of CSA is only caused by the migration of F vacancies.[49] The temperature dependence of the ^{207}Pb-T_1 of $CsPb_{0.9}K_{0.1}F_{2.9}$ is limited (Fig. 9), which could be ascribed to a broad distribution of the correlation time of CSA fluctuation.

Further, the anisotropy of ^{207}Pb-T_1 of $CsPb_{0.9}K_{0.1}F_{2.9}$ was investigated. The broad ^{207}Pb signal at 40 °C was separated into two components: 800–1200 ppm and 1200–1700 ppm. The obtained ^{207}Pb-T_1 values were 0.174(8) s for the former and 0.057(6) s for the latter. As the shorter T_1 value indicates a larger CSA, in this case, the observed high frequency ^{207}Pb shift for $CsPb_{0.9}K_{0.1}F_{2.9}$ compared to that of the $CsPbF_3$ peak correlates with the size of CSA. This shift of ^{207}Pb towards the high frequency region represents a diverse configuration against the 10% K substitution at the Pb sites because the 2D exchange spectrum shows no exchange between the different ^{207}Pb sites (Fig. 8). The large CSA for the high frequency side of ^{207}Pb suggests that the migration of F vacancies is considerably pronounced around Pb, yielding a more distorted local structure near K in $CsPb_{0.9}K_{0.1}F_{2.9}$.

Conclusion

Cubic $CsPb_{0.9}K_{0.1}F_{2.9}$ exhibits an exceptionally low activation energy of 7.9 kJ mol^{-1} for fluoride-ion conductivity. A combination of structural analysis using NPD data and NEB calculations elucidated the conduction mechanism as single F hopping *via* neighbouring vacancies. ^{19}F and ^{207}Pb NMR studies indicated facile migration of the fluoride ions involving F vacancies. The electron density analysis suggested that the fluoride ions migrated *via* an exchange reaction between the Pb 6s lone pairs and fluoride ions. Furthermore, the origin of the mitigated migration barrier was revealed: the localised lone pair in the PbF_5 polyhedron stabilised the saddle-point structure. The low migration energy enabled the retention of high conductivity at 223 K (1.0×10^{-3} S cm^{-1} for bulk conductivity). These findings provide valuable insights into material design for achieving superior ionic conductivity with a low migration barrier for fluoride as well as other anions, such as oxide and chloride.

Author contributions

R. K. designed and directed the project. K. M. and T. S. conducted neutron powder diffraction measurement. M. M. conducted NMR measurement. N. M. conducted first-principles calculations, synchrotron X-ray diffraction, and impedance measurements. N. M. wrote the manuscript in consultation with M. M., K. S., K. S., and R. K. All authors discussed the results and contributed to the final manuscript.

Conflicts of interest

There are no conflicts to declare.

Acknowledgements

This study was conducted using grants from two projects (JPNP16001 and JPNP21006) commissioned by the New Energy and Industrial Technology Development Organization (NEDO). The synchrotron XRD experiments were performed as approved by the Japan Synchrotron Radiation Research Institute (JASRI) (Proposal No. 2020A1645). Neutron diffraction studies were conducted as part of a project approved by the Neutron Scattering Program Advisory Committee of the Institute of Materials Structure Science and KEK (Proposal No. 2019S10). The computational sources of the TSUBAME3.0 supercomputer at the Tokyo Institute of Technology were used. The authors thank Mr Sugihara at the Design and Manufacturing Division, Open Facility Centre, Tokyo Institute of Technology, for manufacturing the sample holder.

References

1 R. Kanno, S. Nakamura, S. Kawamura and Y. Kawamoto, *Solid State Ionics*, 1992, **51**, 53–59.
2 M. Li, M. J. Pietrowski, R. A. De Souza, H. R. Zhang, I. M. Reaney, S. N. Cook, J. A. Kilner and D. C. Sinclair, *Nat. Mater.*, 2014, **13**, 31–35.

3 R. E. Cohen, *Nature*, 1992, **358**, 136–138.
4 R. D. Shannon and R. X. Fischer, *Phys. Rev. B: Condens. Matter Mater. Phys.*, 2006, **73**, 235111–235128.
5 M. A. Kraft, S. P. Culver, M. Calderon, F. Bocher, T. Krauskopf, A. Senyshyn, C. Dietrich, A. Zevalkink, J. Janek and W. G. Zeier, *J. Am. Chem. Soc.*, 2017, **139**, 10909–10918.
6 M. W. Shafer, G. V. Chandrashekhar and R. A. Figat, *Solid State Ionics*, 1981, **5**, 633–636.
7 F. Abraham, J. C. Boivin, G. Mairesse and G. Nowogrocki, *Solid State Ionics*, 1990, **40–1**, 934–937.
8 P. Shuk, H. D. Wiemhofer, U. Guth, W. Gopel and M. Greenblatt, *Solid State Ionics*, 1996, **89**, 179–196.
9 P. Berastegui, S. Hull and S. G. Eriksson, *J. Phys.: Condens.Matter*, 2001, **13**, 5077–5088.
10 M. Uno, M. Onitsuka, Y. Ito and S. Yoshikado, *Solid State Ionics*, 2005, **176**, 2493–2498.
11 L. N. Patro and K. Hariharan, *Solid State Ionics*, 2013, **239**, 41–49.
12 M. A. Reddy and M. Fichtner, *J. Mater. Chem.*, 2011, **21**, 17059–17062.
13 F. Gschwind, G. Rodriguez-Garcia, D. J. S. Sandbeck, A. Gross, M. Weil, M. Fichtner and N. Hormann, *J. Fluorine Chem.*, 2016, **182**, 76–90.
14 K. Mori, A. Mineshige, T. Emoto, M. Sugiura, T. Saito, K. Namba, T. Otomo, T. Abe and T. Fukunaga, *J. Phys. Chem. C*, 2021, **125**, 12568–12577.
15 M. Murakami, F. Fujisaki and Y. Morita, *Solid State Ionics*, 2020, **355**, 115398.
16 S. Hull and P. Berastegui, *J. Phys.: Condens.Matter*, 1999, **11**, 5257–5272.
17 V. Y. Kavun, A. B. Slobodyuk, E. A. Tararako, E. Y. Mikhteeva, V. K. Goncharuk, N. F. Uvarov and V. I. Sergienko, *Inorg. Mater.*, 2005, **41**, 1228–1235.
18 Y. Yamane, K. Yamada and K. Inoue, *Solid State Ionics*, 2008, **179**, 605–610.
19 G. Denes, T. Birchall, M. Sayer and M. F. Bell, *Solid State Ionics*, 1984, **13**, 213–219.
20 A. Walsh, D. J. Payne, R. G. Egdell and G. W. Watson, *Chem. Soc. Rev.*, 2011, **40**, 4455–4463.
21 S. F. Matar and J. Galy, *Solid State Sci.*, 2016, **52**, 29–36.
22 F. Fujisaki, K. Mori, M. Yonemura, Y. Ishikawa, T. Kamiyama, T. Otomo, E. Matsubara and T. Fukunaga, *J. Solid State Chem.*, 2017, **253**, 287–293.
23 T. Birchall, G. Dénès, K. Ruebenbauer and J. Pannetier, *Hyperfine Interact.*, 1986, **29**, 1331–1334.
24 G. Dénès, M. C. Madamba, H. Merazig, A. Muntasar and Z. Zhu, *AIP Conf. Proc.*, 2016, **1781**, 020006.
25 J. Z. Wang, J. P. Hao, C. M. Duan, X. C. Wang, K. Wang and C. Ma, *Small*, 2022, **18**, 2104508.
26 S. Kawaguchi, M. Takemoto, K. Osaka, E. Nishibori, C. Moriyoshi, Y. Kubota, Y. Kuroiwa and K. Sugimoto, *Rev. Sci. Instrum.*, 2017, **88**, 085111.
27 M. Yonemura, K. Mori, T. Kamiyama, T. Fukunaga, S. Torii, M. Nagao, Y. Ishikawa, Y. Onodera, D. S. Adipranoto, H. Arai, Y. Uchimoto and Z. Ogumi, *J. Phys.: Conf. Ser.*, 2014, **502**, 012053.
28 R. Oishi, M. Yonemura, Y. Nishimaki, S. Torii, A. Hoshikawa, T. Ishigaki, T. Morishima, K. Mori and T. Kamiyama, *Nucl. Instrum. Methods Phys. Res., Sect. A*, 2009, **600**, 94–96.
29 F. Izumi and K. Momma, *Solid State Phenom.*, 2007, **130**, 15–20.
30 Y. Ishikawa, J. R. Zhang, R. Kiyanagi, M. Yonemura, T. Matsukawa, A. Hoshikawa, T. Ishigaki, S. Torii, R. Oishi-Tomiyasu and T. Kamiyama, *Phys. B*, 2018, **551**, 472–475.
31 W. S. Brey and M. L. Brey, in *Encyclopedia of Nuclear Magnetic Resonance*, John Wiley and Sons, Inc., Chichester, 1996, vol. 3, pp. 2063–2071.
32 A. Bielecki and D. P. Brum, *J. Magn. Reson., Ser. A*, 1995, **116**, 215–220.
33 J. Jeener, B. H. Meier, P. Bachmann and R. P. Ernst, *J. Chem. Phys.*, 1979, **71**, 4546–4563.
34 K. Takeda, *J. Magn. Reson.*, 2008, **192**, 218–229.
35 P. E. Blochl, *Phys. Rev. B: Condens. Matter Mater. Phys.*, 1994, **50**, 17953–17979.
36 J. P. Perdew, A. Ruzsinszky, G. I. Csonka, O. A. Vydrov, G. E. Scuseria, L. A. Constantin, X. L. Zhou and K. Burke, *Phys. Rev. Lett.*, 2008, **100**, 136406.
37 G. Kresse and J. Furthmuller, *Phys. Rev. B: Condens. Matter Mater. Phys.*, 1996, **54**, 11169–11186.
38 G. Kresse and J. Hafner, *Phys. Rev. B: Condens. Matter Mater. Phys.*, 1993, **48**, 13115–13118.
39 J. Heyd, G. E. Scuseria and M. Ernzerhof, *J. Chem. Phys.*, 2003, **118**, 8207–8215.
40 J. Heyd, G. E. Scuseria and M. Ernzerhof, *J. Chem. Phys.*, 2006, **124**, 219901–219906.
41 J. Paier, M. Marsman, K. Hummer, G. Kresse, I. C. Gerber and J. G. Angyan, *J. Chem. Phys.*, 2006, **125**, 249901–249902.
42 K. Momma and F. Izumi, *J. Appl. Crystallogr.*, 2008, **41**, 653–658.
43 M. Gombotz, I. Hanghofer, S. Eisbacher-Lubensky and H. M. R. Wilkening, *Solid State Sci.*, 2021, **118**, 106680.
44 A. Kojima, K. Tozaki, T. Ogawa, T. Takizawa and T. Kanashiro, *J. Phys. Soc. Jpn.*, 1988, **57**, 176–187.
45 C. C. Stoumpos, C. D. Malliakas and M. G. Kanatzidis, *Inorg. Chem.*, 2013, **52**, 9019–9038.
46 A. Walsh and G. W. Watson, *J. Solid State Chem.*, 2005, **178**, 1422–1428.
47 R. D. Shannon, *Acta Crystallogr., Sect. A: Found. Adv.*, 1976, **32**, 751–767.
48 C. Brevard and P. Granger, *Handbook of High Resolution Multinuclear NMR*, Wiley, New York, 1981.
49 M. Murakami, Y. Morita and M. Mizuno, *J. Phys. Chem. C*, 2017, **121**, 2627–2634.

